

Article

Exploration Targeting in the Shadan Porphyry Gold–Copper Deposit, Lut Block, Iran: Analysis of Spatial Distribution of Sheeted Veins and Lithochemical Data

Davood Raeisi ^{1,*}, Saeid Hajsadeghi ² , Elham Hosseinzadehsabeti ³ , Shahrouz Babazadeh ⁴, David R. Lentz ⁵  and M. Santosh ⁶

¹ School of Geology, College of Science, University of Tehran, Tehran 14155-6455, Iran

² School of Mining Engineering, College of Engineering, University of Tehran, Tehran 14155-6455, Iran

³ Independent Researcher, Salt Lake City, UT 84112, USA

⁴ Research Institute for Earth Sciences, Geological Survey of Iran, Tehran 13185-1494, Iran

⁵ Department of Earth Sciences, University of New Brunswick, Fredericton, NB E3B 5A3, Canada

⁶ School of Earth Science and Resources, China University of Geosciences, Beijing 100083, China

* Correspondence: d.raeisi@ut.ac.ir

Abstract: The Lut Block is a potential porphyry-style mineralized region in Iran including the well-explored Shadan porphyry gold-copper deposit, which has an extensive zone of gold- and copper-bearing stockwork-like sheeted veins. The structural setting of this deposit is a key to understanding the genesis of the mineralization. Our field studies show that the mineralization occurs as steeply dipping ore bodies along NW–SE transpressional faults. The zones with a high frequency of veins and volume of veins have a NW–SE trend, which is closely related to transpressional faults. We propose that such a compressional regime inhibits focused ore-forming fluid flow to higher levels in the crust. After a local change in stress field, fluid depressurization and channeling along transpressional faults generated the sheeted veins. This indicates an important role of these transpressional faults in focusing and controlling mineralization within this porphyry deposit, which has important implications for the exploration of porphyry deposits on a regional scale. The spatial distribution of sheeted veins is used to examine gold anomalies from lithochemical data extracted by fractal models. The results show that a combination of high vein density and high vein volume areas with gold anomalies could result in identifying areas with greater potential at the deposit to regional scale.

Keywords: Shadan; porphyry gold–copper deposit; exploration targeting; fractal model



Citation: Raeisi, D.; Hajsadeghi, S.; Hosseinzadehsabeti, E.; Babazadeh, S.; Lentz, D.R.; Santosh, M. Exploration Targeting in the Shadan Porphyry Gold–Copper Deposit, Lut Block, Iran: Analysis of Spatial Distribution of Sheeted Veins and Lithochemical Data. *Minerals* **2023**, *13*, 471. <https://doi.org/10.3390/min13040471>

Received: 2 January 2023

Revised: 28 February 2023

Accepted: 3 March 2023

Published: 27 March 2023



Copyright: © 2023 by the authors. Licensee MDPI, Basel, Switzerland. This article is an open access article distributed under the terms and conditions of the Creative Commons Attribution (CC BY) license (<https://creativecommons.org/licenses/by/4.0/>).

1. Introduction

Mineral exploration targeting is an important tool particularly in cases where exposed ore deposits are rare. Mineral potential mapping (hereafter MPM) methods are more effective when using conceptual mineral deposit models and data available to support exploration targeting. Building on the research work on mineral systems, ref. [1] presented a new exploration information system to help explore the complex natural phenomena that can play a key role in exploration targeting. However, conceptual models should be carefully used in translating key criteria into effective exploration targeting maps. For example, high density lineaments are generally considered as promising zones that utilize potential targeting elements in MPM studies for prioritizing drill hole positioning for finding and evaluation various porphyry-type deposits [1–4]. Lineament density can be mapped from geological data, geophysical data, or remote sensing studies through three methods, namely visual, semi-automatic, and automatic. Apart from the advantages of these methods, there are still several shortcomings in using lineament density as an element in MPM. Fault data are almost never attributed in terms of fault type and age. Furthermore, all faults do not act as permeable pathways for the transportation and localization of

hydrothermal fluids (e.g., post-mineralization faults). In this context, there is a need to emphasize fracture generation and distribution to highlight its role in facilitating the transport of ore-forming fluids within a porphyry deposit setting.

Porphyry deposits are characterized by numerous generations of fractures from pre-mineralization to syn-mineralization, and to many post-mineralization sets. Fractures can be distinguished by mineral infill and alteration assemblages (e.g., [5,6]). Inside mineralized intrusions and their surroundings, the formation of brittle fractures and veins is controlled by magma emplacement dynamics coupled with crystallization, the fluctuation of pressurized fluids, changing physiochemical conditions, and the tectonic evolution of the local and regional stress fields [7–9]. The distribution of alteration and mineralization is controlled by fractures, as well as macroscopic cracks and fractures that developed after ore formation [5].

Fracture formation in a porphyry deposit is controlled by numerous factors including the inherited host rock structure (e.g., mechanical anisotropy), major changes in ambient stress field, episodic magma intrusion and cooling, and fluctuation in the hydraulic pressure of the system [10]. Fracture orientations result either during the formation of the host rock or during the mineralization. The two major processes associated with formation of veins associated with porphyries are hydraulic processes and the local tensional stresses of the host rock [7]. The local stretching of the host rock could be a function of deformation and strain [11–13].

The well-established conceptual models visualize a local extension within a far-field regional stress regime governed by the overall regional-scale compression in which porphyry copper–gold deposits are generally emplaced. This facilitates the transition of magma from the MASH zone (i.e., melting, assimilation, storage, homogenization) en-route to the surface (e.g., [14–17]). In such structurally dynamic conditions, porphyry deposits are characterized by stockwork and hydrothermal breccia mineralization. Combinations such as those described above are considered most prevalent in pull-apart basins that have been released by strike-slip faults [18–20]. Strike-slip faults are used as a key exploration feature in locating porphyry deposits.

The Urumieh-Dokhtar magmatic arc (UDMA) in the Alpine–Himalayan (Tethyan) orogenic belt is an important host of porphyry deposits including the Sarcheshmeh, Sungun, and Meiduk deposits (Figure 1). Analysis of the fault kinematics data in the UDMA reveal an association between porphyry deposits and the extensional fault duplex pattern [21–23]. These extensional fault duplex patterns imply that dilatational zones, which are followed by NW–SE trending dilatational normal faults, are optimal for the porphyry deposit emplacement [23].

The Lut Block as part of the central Iran micro-continent is an important host of porphyry deposits and prospects, especially the Shadan [24,25] and Maher Abad [26] deposit systems (Figure 1). The Shadan Au–Cu deposit is a suite of sheeted vein mineralization that cannot satisfactorily be explained by the model attributed to the UDMA. Sheeted veins, as dilatant structures, act to transfer ore-forming fluids from a deeper level but hypabyssal magmatic source to shallower crustal levels, where mineralization occurs either inside intrusive stocks (endocontact) or in direct contact with host rock (exocontact).

In this study, we mapped and analyzed sheeted veins to decipher the spatial distribution of fracture mesh related to porphyry deposit, which helps lead to insights for vein formation and a revised structural model to enhance our understanding of the fundamental controls on mineralization. Advancing a structural model is important in formulating the criteria for porphyry deposit targeting in this region. Furthermore, an integration of the spatial distribution of fracture mesh and lithogeochemical data helps in identifying the potential areas for exploratory drilling.

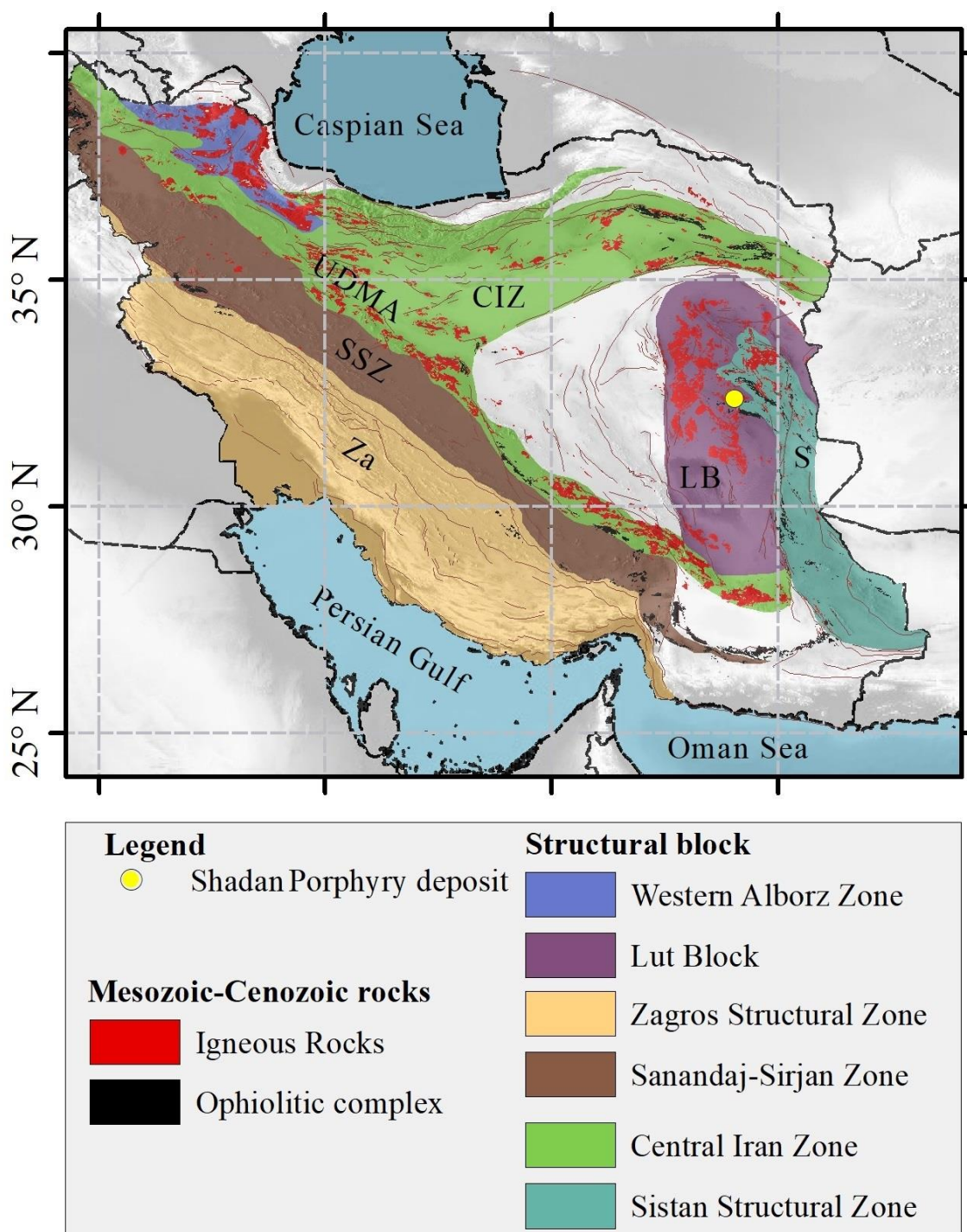


Figure 1. Location of key porphyry deposits on lithologic structural map of Iran.

2. Geological Setting

2.1. Regional Geology

The Shadan porphyry Au–Cu deposit is located in the volcano-plutonic suites of the Lut Block, a segment in the central part of the Alpine–Himalayan Belt (Figure 1; [27–30]). The Lut Block is exposed over an area of ca. 900 × 200 km, extending N–S and trending from the Doruneh Fault to the Jazmorian basin [31]. The Lut Block spans a wide spectrum of rocks composed of a pre-Jurassic metamorphic-sedimentary basement, Jurassic volcano-sedimentary rocks, and Meso-Cenozoic igneous rocks (Figure 2) [32,33]. Previous studies in this region suggest initiation of magmatic activity during Jurassic [34]. Discontinuous sub-

duction along the Lut Block during upper Cretaceous (ca. 75 Ma) and Eocene (ca. 47–30 Ma) is considered to have generated alkaline, including shoshonitic magmatism [34].

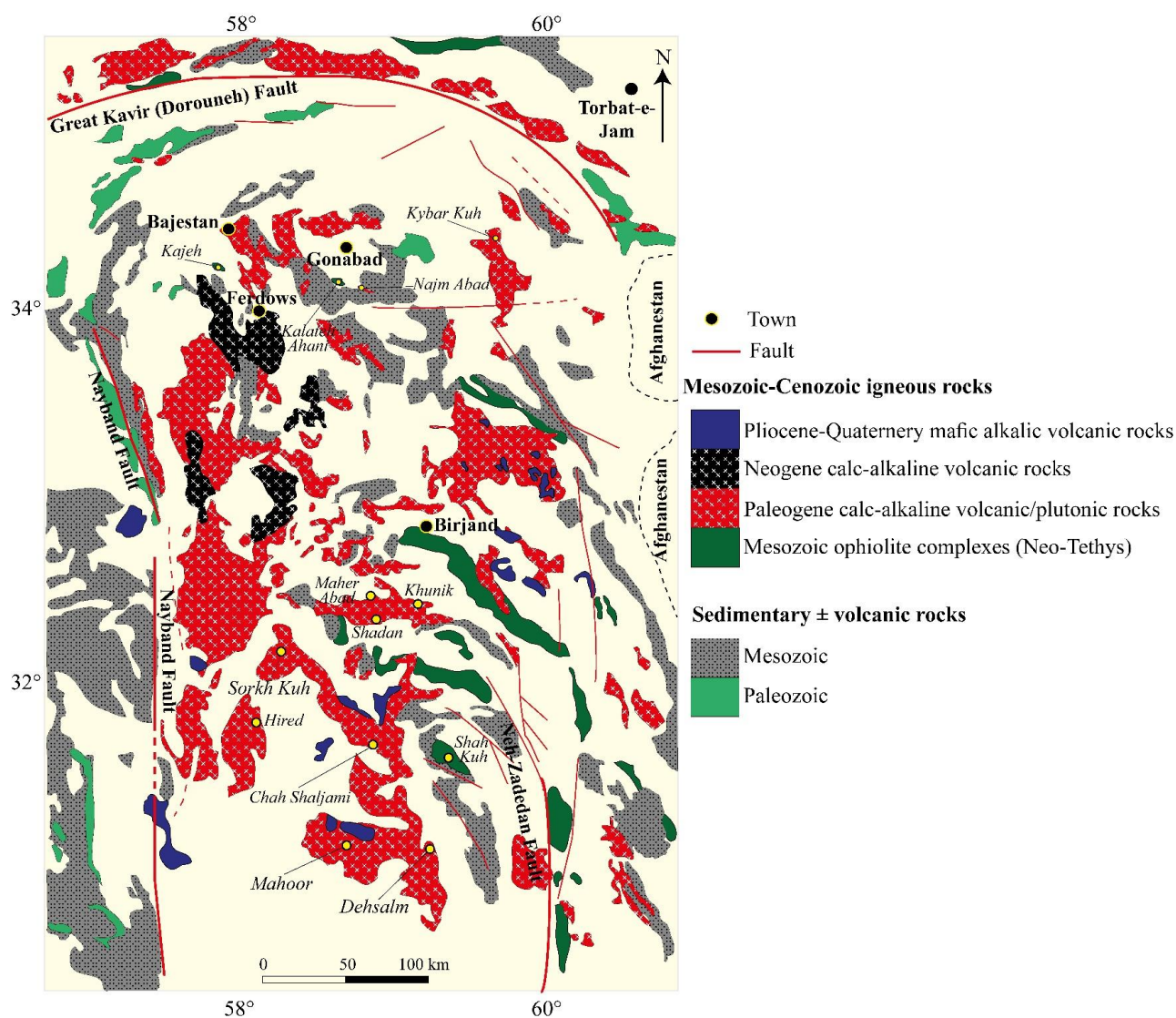


Figure 2. Geology of the Lut Block, eastern Iran, modified from [24].

Considerable debate surrounds the tectono-magmatic setting of the Lut Block. The influence of active tectonic forces along with subduction in an extensional tectonic setting has been rejected by many authors (e.g., [35–43]). Paleogene magmatism of eastern Iran is a frame of overwhelming magmatic flare-up as a result of NE-ward subduction of the Neo-Tethys Ocean beneath central Iran [35]. By contrast, ref. [36] attributed the subducted oceanic lithosphere beneath the Afghan Block as the trigger of magmatism and the related mineralization in ophiolitic complex between the Lut and the Afghan continental blocks, eastern Iran. Several studies support a continental arc tectonic setting, as their conclusions were inferred from westward subduction of the Sistan Ocean beneath the Lut Block (e.g., [37–43]).

2.2. Deposit Geology

The Shadan deposit contains 27 Mt and 0.55 g/t Au [44] and has been classified as an Au–Cu porphyry deposit due to the low content of Cu mineralization, i.e., a low Cu/Au ratio of ~ 0.27 ($\frac{\text{wt}\%}{\text{g/t}}$) (Figure 3). The geological features of the Shadan deposit were studied by [24]. The mineralization occurs as a few hundred-meter ore body that is associated

with pipe-like intrusions, which extend vertically over several hundred meters (Figure 4). The Shadan gold–copper deposit is hosted by calc-alkaline intrusions with an adakitic signature with the porphyritic intrusions emplaced into volcanic and volcanoclastic rocks at 37.26 ± 0.30 Ma, based on Ar–Ar biotite geochronology [24]. Monzonite to monzodiorite, diorite, microdiorite, and monzodiorite dykes intruded into the Eocene Oligocene intermediate to acidic lava flows as andesite, rhyolite, and rhyolitic tuff (Figure 5). Andesite and tuff are the primary country rocks. Andesite varies from dark green to black and is porphyritic, containing between 20% and 50% phenocrysts including plagioclase, biotite, and amphibole. Phenocrysts of biotite and amphibole are mostly replaced by hydrothermal biotite and magnetite. The monzonite to monzodioritic porphyry shows phenocrysts (up to 40–50 vol. %) of plagioclase, quartz, and alkali feldspar. The phenocrysts are set in a fine-grained groundmass. The plagioclase phenocrysts are predominantly euhedral–subhedral with complex compositional zoning.

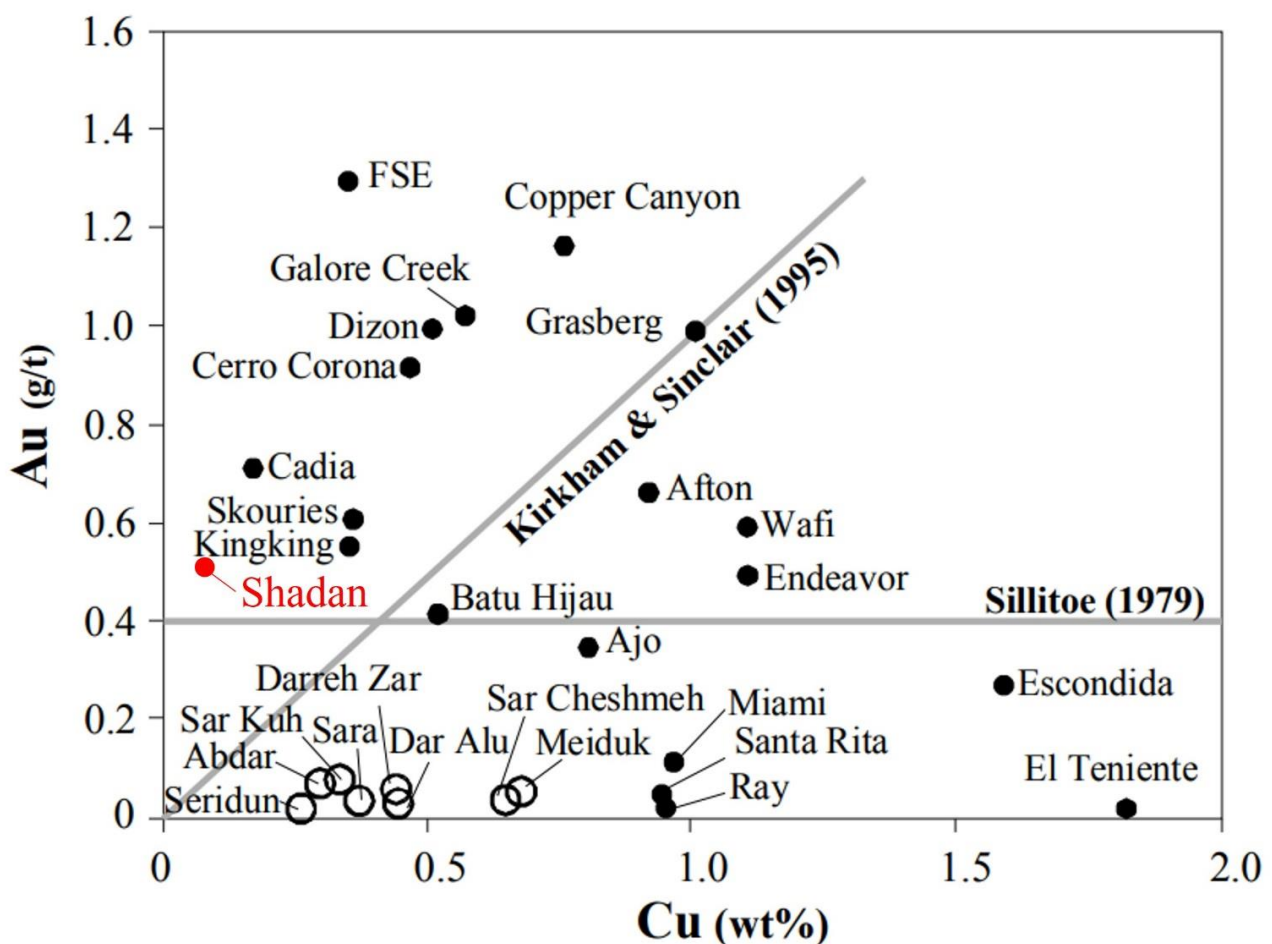


Figure 3. Location of the Shadan porphyry (red circle) compared with Kerman porphyry copper deposits (open circles) [45] on Cu vs. Au diagram on which the porphyry Cu–Au deposits are plotted above the diagonal line of [46] and the horizontal line of [47].

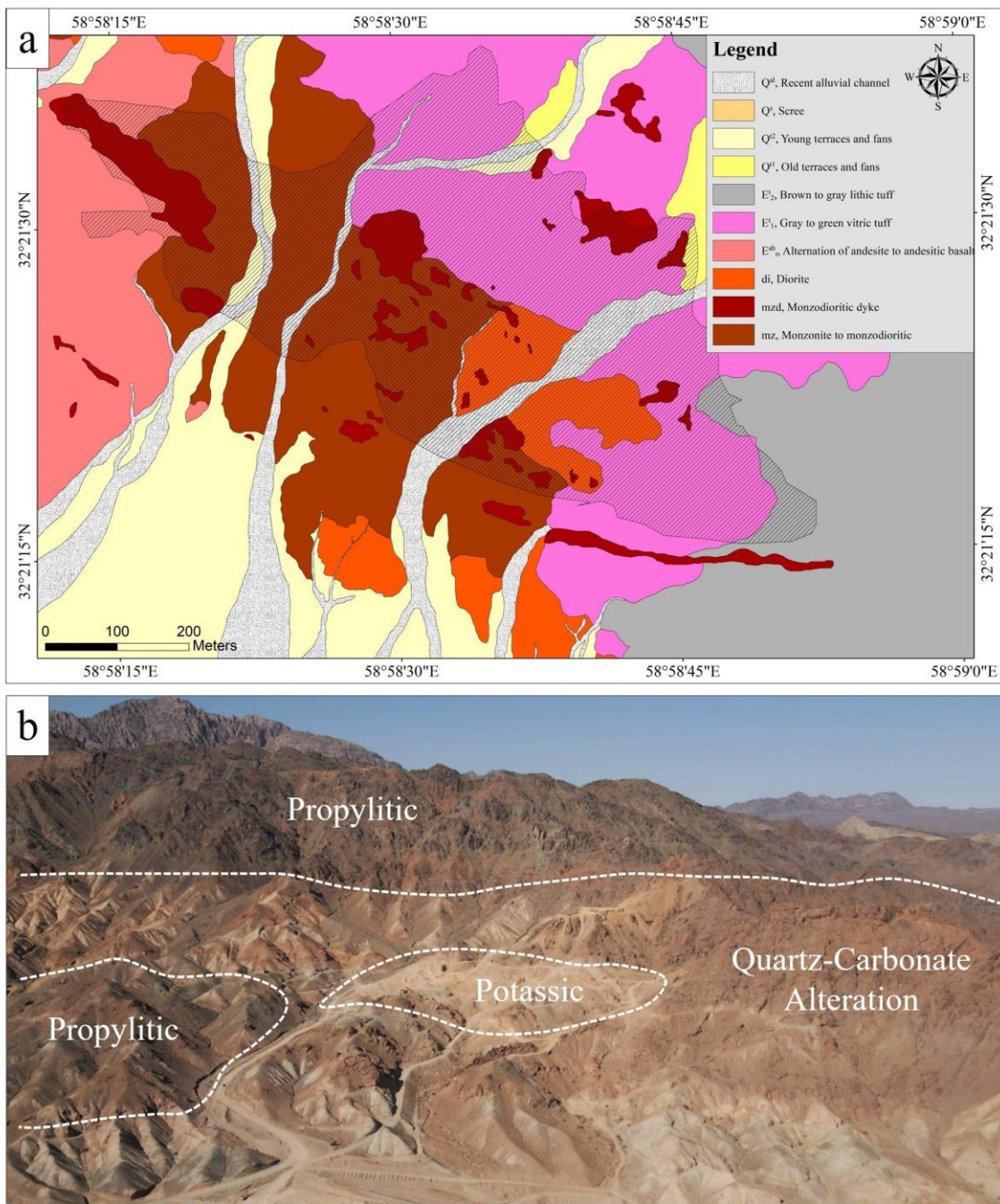


Figure 4. (a) Local geological map of Shadan porphyry gold–copper deposit. Zone of sheeted vein indicated by cross-hatching. (b) Aerial view of the Shadan porphyry, NW–SE mineralization zone indicated by light-colored intrusive rocks, surrounded by propylitically altered volcanic rocks.

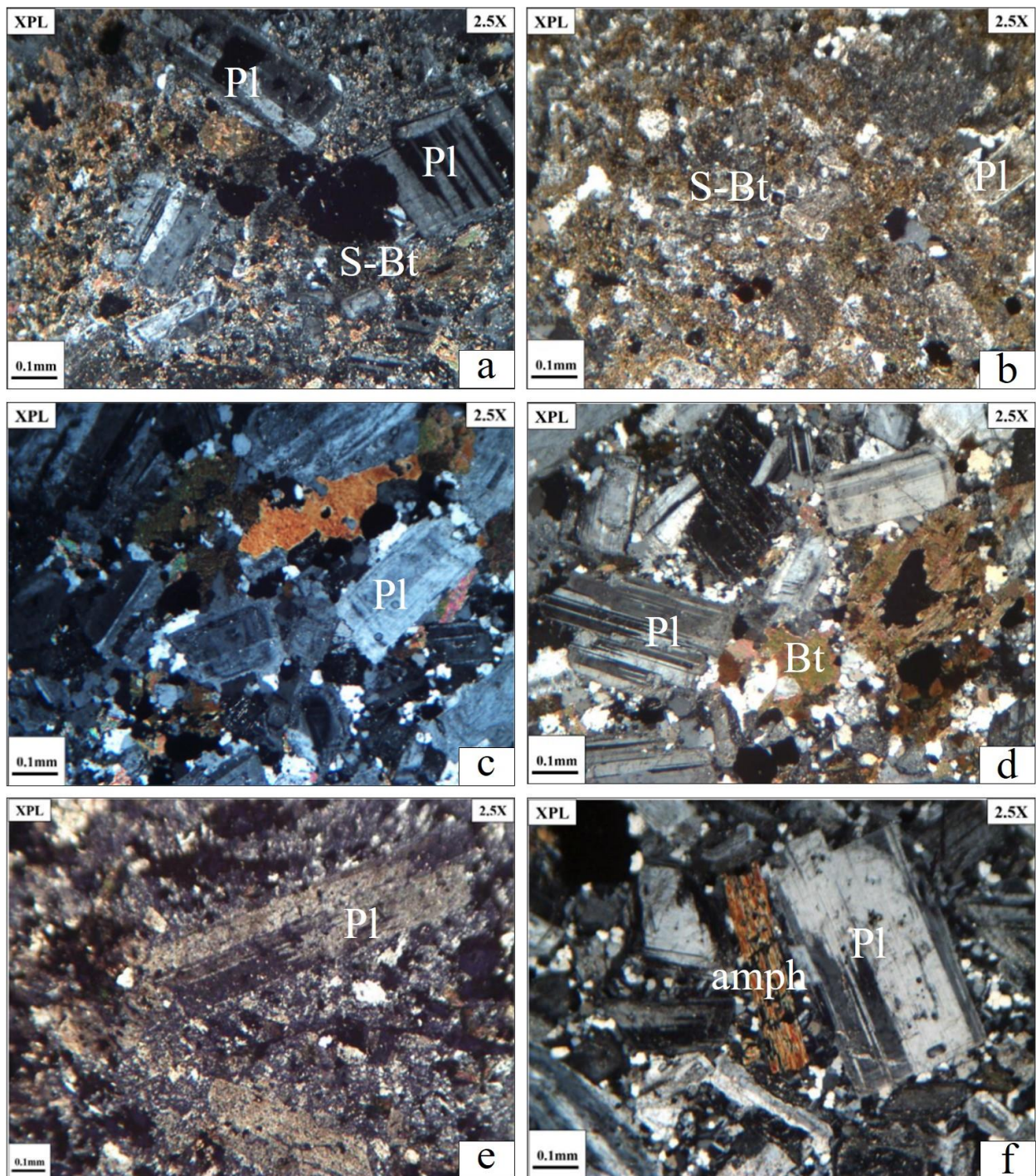


Figure 5. Photomicrographs of selected rocks from Shadan in cross polarized transmitted light. (a,b) Mineral assemblages of plagioclase and secondary biotite (originally phenocrysts in a microcrystalline groundmass) in andesite. (c) Mineral assemblages of phenocrysts of plagioclase, hornblende, and quartz with a minor groundmass component in quartz diorite. (d) Phenocryst assemblages of medium-grained plagioclase, quartz, and secondary biotite in diorite. (e) Medium-grained monzonite with quartz, plagioclase, and alkali feldspar phenocrysts-rich assemblage. (f) Phenocrysts of plagioclase, alkali feldspar, and quartz in monzodiorite. Abbreviations: Pl = plagioclase; S-Bt = secondary biotite; Bt = biotite; Amph = amphibole.

The diorite is characterized by the presence of phenocrysts of medium-sized plagioclase, biotite, and hornblende with a medium-grained groundmass. Magmatic biotite and

hornblende phenocrysts have generally been replaced by biotite and commonly associated with hydrothermal magnetite.

3. Hydrothermal Alteration and Mineralization

Mineralogically and spatially, different alteration types have affected the volcano-plutonic rocks in the Shadan deposit consisting of potassic, phyllic, propylitic, argillic, and quartz-carbonate alteration (Figure 6). Initially, potassic alteration occurred within subvolcanic intrusions, indicated by local secondary orthoclase, magnetite, and biotite assemblages. Magnetite occurs as veinlet and massive replacements in potassic and phyllic alteration. Orthoclase formed along the margins of magnetite veinlets. Magnetite patches occur in andesitic host rock due to the replacement of biotite phenocrysts by magnetite [48,49].

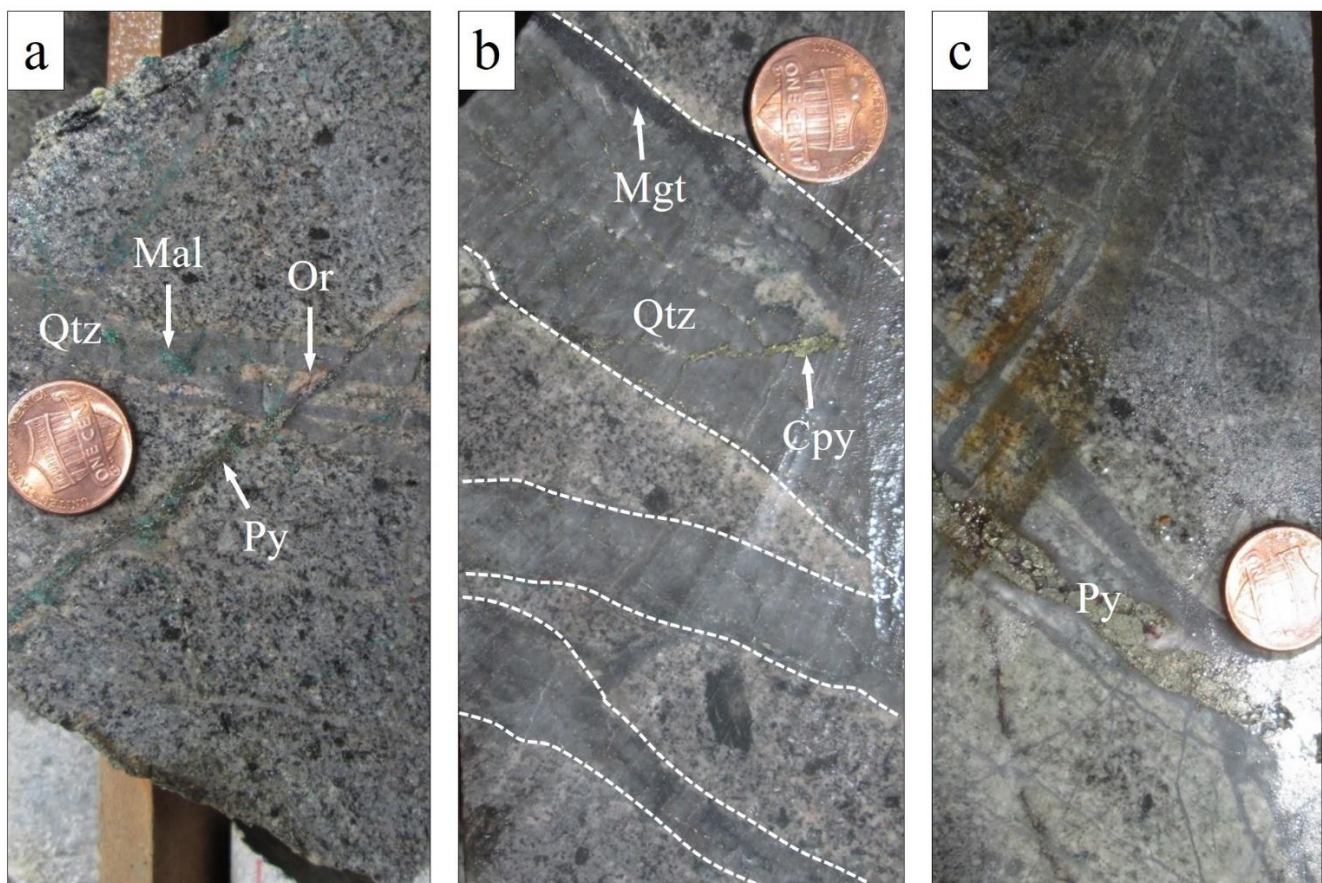


Figure 6. Photographs of (a) drill core sample of orthoclase veinlet in monzodiorite as potassic alteration, quartz veinlet crosscut by pyrite veinlet; (b) magnetite- and chalcopyrite-bearing quartz veinlet; (c) quartz veinlet crosscut by anhydrite veinlet in potassically altered andesite host rock. Abbreviations: Mal = malachite; Or = orthoclase; Py = pyrite; Mag = magnetite; Cpy = chalcopyrite; Qtz = quartz.

Propylitic alteration is widely observed at the surface outcrops. The mineral assemblages within the propylitic alteration zone are typically characterized by the replacement of ferromagnesian phenocrysts and groundmass with chlorite and local epidote or calcite. The replacement of plagioclase by calcite is quite common in this zone. The phyllic alteration is widely observed at the center of the area, and variably overprints earlier formed potassic and propylitic alteration. Phyllic alteration is determined by quartz, sericite, and sometimes pyrite. Copper mineralization occurs as sulfide, such as chalcopyrite and minor bornite. Finally, argillic alteration with a white to bright grey cream color was observed at

the surface. This alteration is determined by clay minerals, especially montmorillonite and kaolinite. Additionally, tourmalinization occurs in a restricted area around the silicification in the Shadan porphyry system.

Gold and copper mineralization in the Shadan deposit is closely related to the multiple-stage porphyry intrusion. Monzonite to monzodiorite are the main host rocks for gold and copper mineralization. Gold and Cu-Fe sulfides are hosted by quartz \pm anhydrite sheeted veins. Mineralization occurs as a steeply dipping ore body that is controlled along NW–SE faults, with an extensive zone of sheeted veins.

4. Methods

The structural setting of mineralization in porphyry deposits can be investigated by systematic mapping of fracture and vein characteristics, as well as various sets of faults [10,11]. Measuring vein sets in comparison to single veins permitted us to achieve a statistically representative dataset. The character of each vein set, including dip, dip direction, vein spacing, and vein thickness, was recorded using compass and ruler for a meter window along a traverse.

For vein spacing and vein thickness, total vein density (V.D) per meter, and the total vein volume (V.V) per meter, calculate as follows [10]:

$$\text{Total vein density} = \frac{1}{\text{vein spacing(m)}} \quad (1)$$

$$\text{Total vein volume} \approx \Sigma_n[\text{mean vein thickness} \times \text{total vein density per meter}] \quad (2)$$

The lithochemical data were collected from surface geological and geochemical surveying on a NW–SE regular grid by 90 m \times 90 m distancing conducted as an exploration program by Rio Tinto. The 360 lithochemical samples were digested by a HF-multi acid method and analyzed by fire assay for Au.

Fractal models, presented by Mandelbrot (1983), have been used in many different cases to explain geological and mineralization processes. Considering spatial information of mineral deposit data, it can be noted that fractal models are useful tools which reveal the relationships among geological, geochemical, and mineralogical settings [50–54]. Famous fractal models include number–size (N–S: [55,56]), concentration–area (C–A: [57]), spectrum–area (S–A: [58]), concentration–distance (C–D: [59]), concentration–volume (C–V: [60] Afzal et al. 2011), concentration–number (C–N: [61]), and simulated size–number (SS–N: [62]).

Concentration–number (C–N) fractal model is one of the fractal models [55] which is used to separate geochemical background and anomaly in a geochemical dataset. The model is defined as (1):

$$N(\geq \rho) \propto \rho^{-\beta} \quad (3)$$

where $N(\geq \rho)$ denotes the sample number with concentration values greater than ρ value, ρ is the concentration of an element, and β is the fractal dimension. The main advantage of this method is the classification of geochemical populations before their estimation [56,63].

5. Results

5.1. Quartz Vein Morphology

Quartz sheeted veins at Shadan are thin and composed of crystalline quartz veinlets to thicker (up to 5 cm) quartz veins with distinct rhombohedral crystals. Contacts between quartz veins and the wall rock are sharp (Figure 7). They are mostly sub-vertical sheeted vein sets with a NW–SE trend. Shallowly dipping veins were commonly developed early in the vein paragenesis.

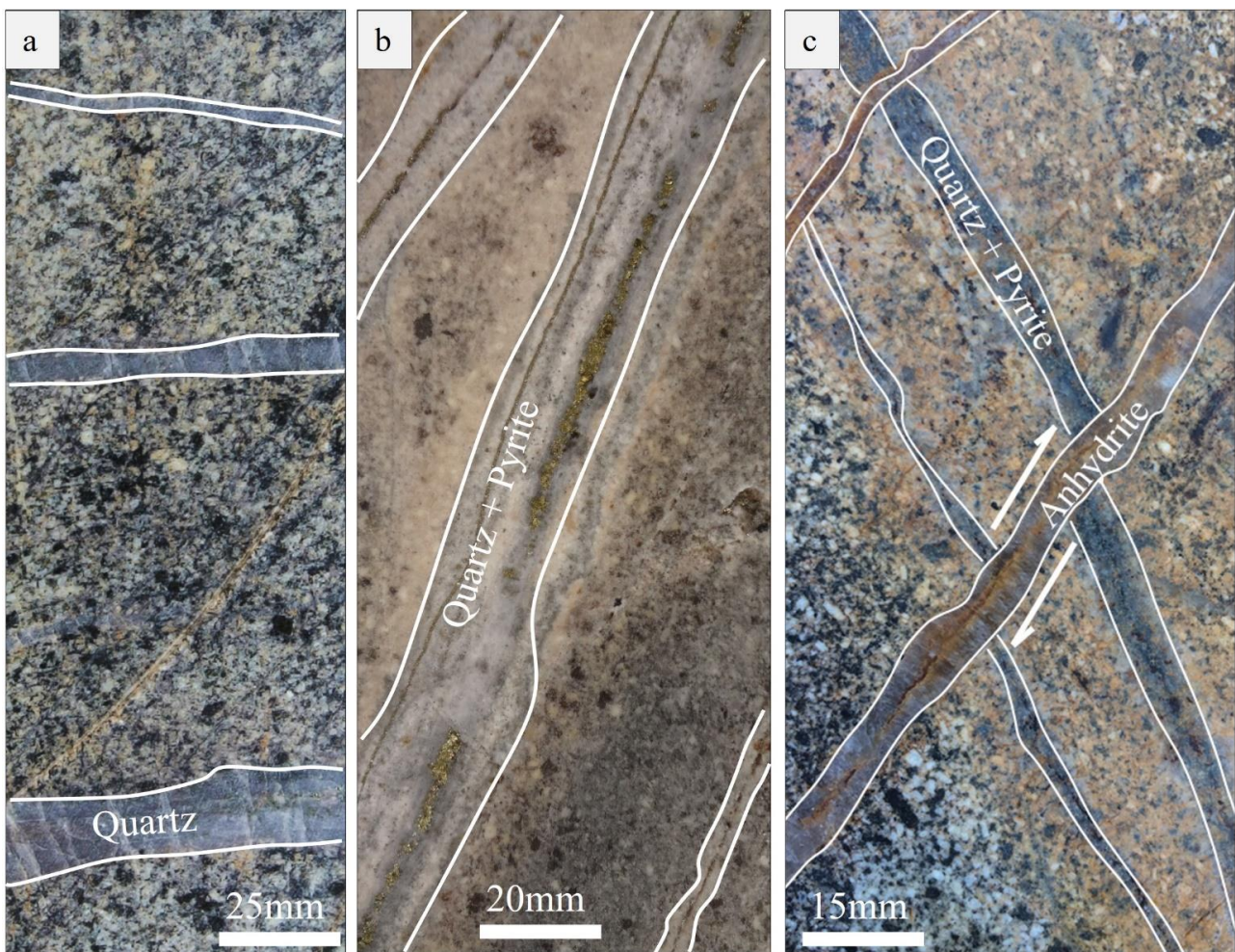


Figure 7. Photographs of veins from drill core with porphyry hosts; (a) flat dipping barren quartz sheeted vein; (b) steep dipping quartz-pyrite sheeted vein with discontinuous bleached halo; (c) steep dipping quartz-pyrite sheeted vein with halo (earthy brown) crosscut by steep dipping anhydrite sheeted vein.

5.2. Fault Orientation and Distribution

The Shadan faults typically show a high dip angle (60–80°) with northwest and east–west trends (Figure 8a). Some are curvilinear extending over 100 m. Subordinate, smaller (>50 m) faults also trend north–northwest and west with a moderate dip angle (40–60°). The deposit is dominated by northwest-trending transpressional faults. Such a fault system indicates a compressional regime where σ_1 is along NE–SW. NE–SW faults can be interpreted as misoriented faults. The term “misoriented fault” refers to the faults that have an orientation not optimal for the aperture with respect to the stress field. These orientations are perpendicular to the maximum stress axis (σ_1) and parallel to the minimum stress axis (σ_3) [64].

5.3. Quartz Vein Orientation, Density, and Volume

A total of 714 vein sets were documented at the Shadan deposit. Quartz veins are typically dominated by sub-vertical and sub-horizontal sheeted vein sets; however, no systematic radial distribution is evident. The sheeted veins with a preferred orientation of 315° to 345° are the dominant veins across the studied area (Figure 8b). Vein widths and orientation relationship has been investigated using a weighted width-azimuth plot. The plot can show the direction with maximum cumulative vein thickness. The weighted width-azimuth plot shows a preferred maximum cumulative thickness for orientations at

$\sim 340^\circ$ to 360° (Figure 8c). Thin veins (commonly referred to as stockwork) have a lower cumulative width in comparison to sheeted veins. An equal-area stereographic projection plot shows that the veins are mostly sub-vertical (Figure 8d), whereas a small number of veins are shallow dipping, sub-horizontal veins.

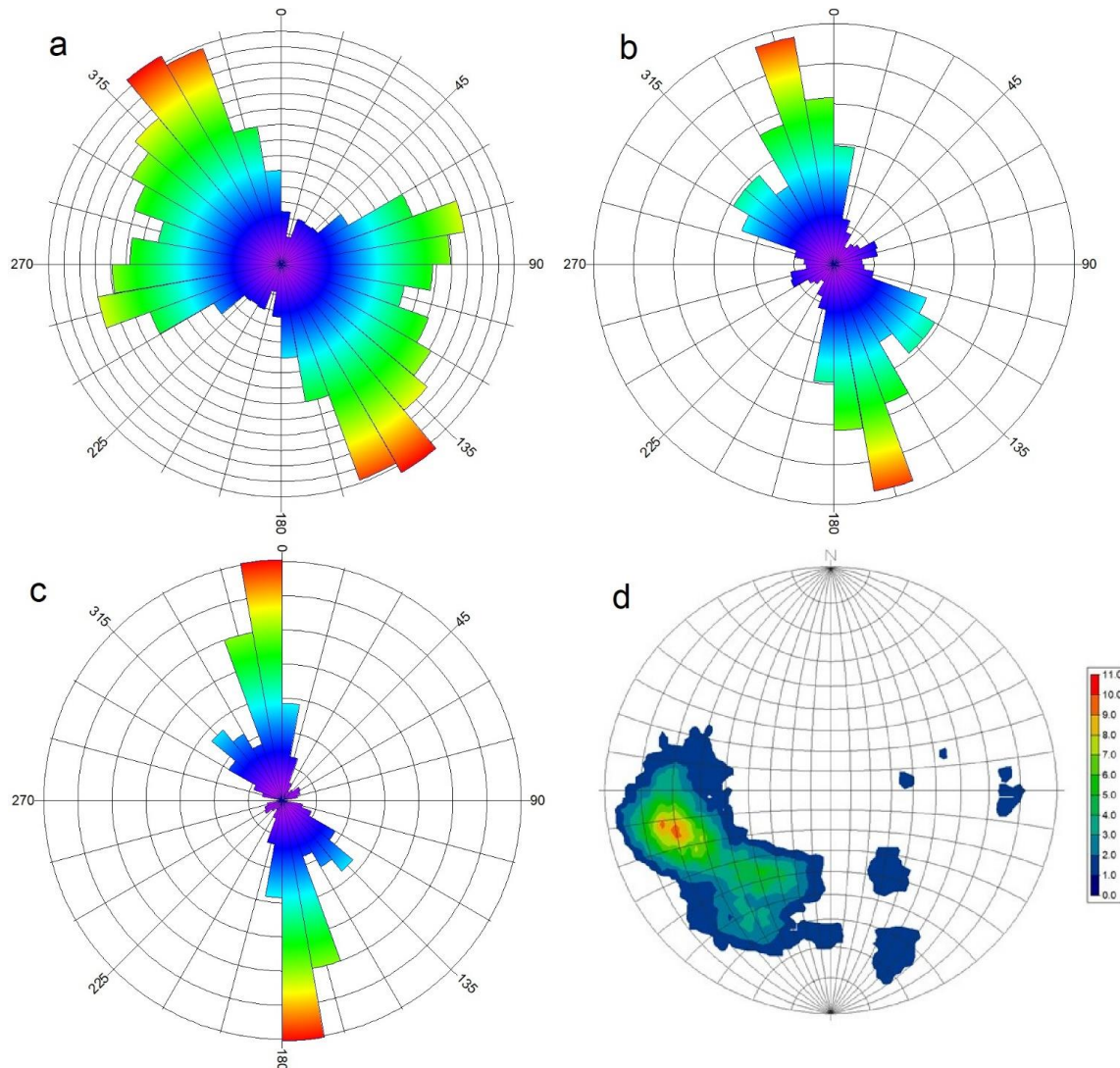


Figure 8. (a) Orientation of faults at Shadan on a rose diagram; (b) orientation of quartz veins and vein sets at the Shadan deposits on a rose diagram; (c) width-azimuth rose diagram plot of all quartz illustrating a strong preferred orientation. This plot is constructed in order to reduce the data scatter caused by the thin networked veins; (d) orientation data extrapolated from vein sets measured are plotted on a stereonet. Note the presence of a general northwest vein trend as shown on the equal area stereographic projection of contoured poles to quartz veins. This plot shows that the majority of veins are near vertical.

Contoured plots were used to analyze the total quartz vein frequency (Figure 9a) and total vein volume (Figure 9b). High total vein frequency was distinguished as NW–SE trending zones along porphyry intrusions (Figure 9a). As total vein frequencies, total vein volume shows a NW–SE trend (Figure 9b). Both vein frequency and vein volume are consistent across the deposit, decreasing into low-grade mineralization. Notably, the vein frequency shows a positive correlation with vein volume. Thus, the zone of high vein volume is defined by thick sheeted veins (up to 30 mm). The zone of thin stockwork (less than 5 mm) veins has a lesser vein volume and vein frequency than those of sheeted zones. Gold–copper grade correlates with both vein frequency and vein volume, indicating

same mineralizing potential of both stockwork and sheeted veins. The other interesting point is demonstrating a positive association between Au mineralization and increasing the number of veins in the investigated region. The high vein frequency and vein volume zones are closely related to transpressional faults.

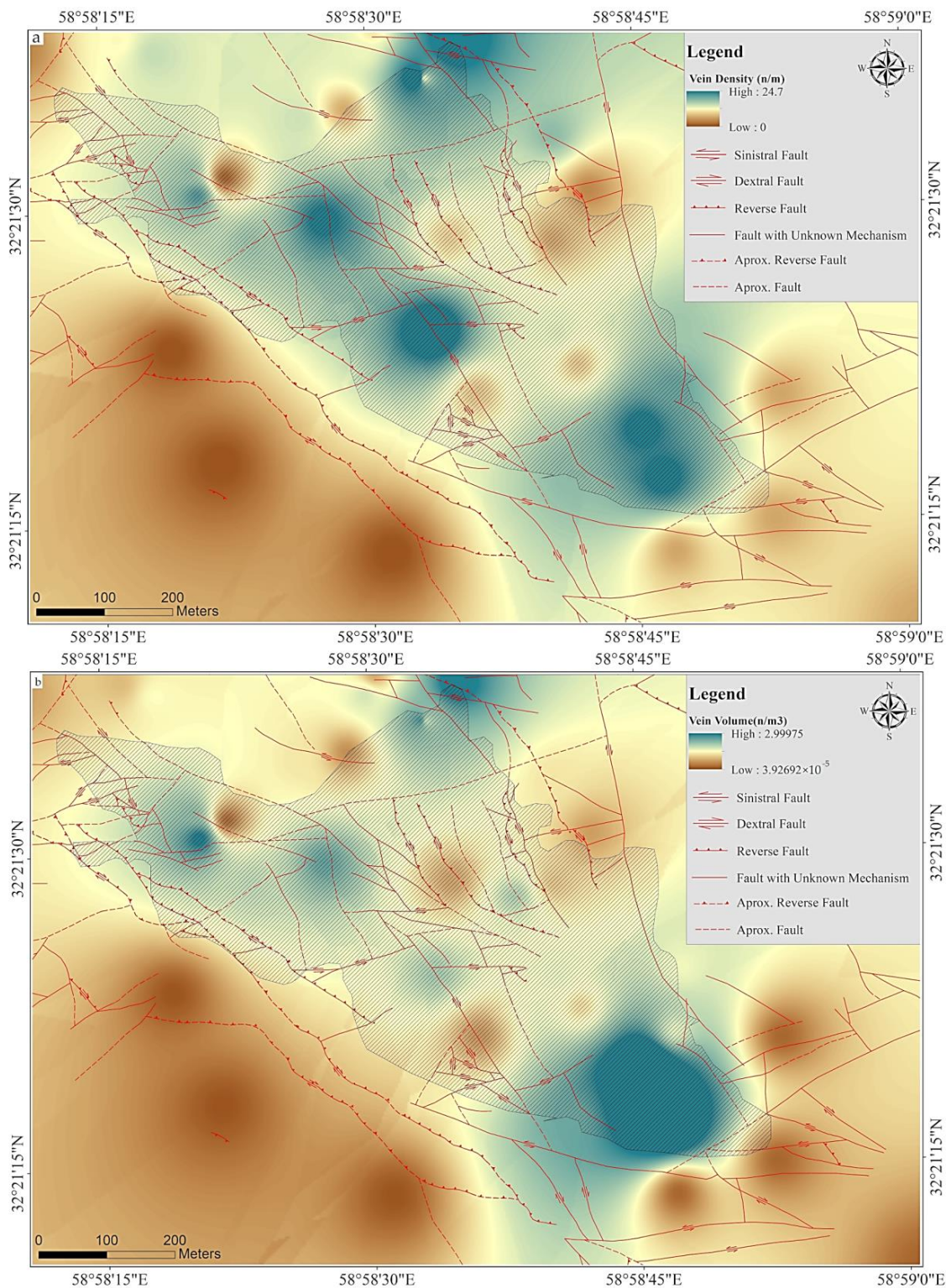


Figure 9. (a) Contour plot of the total vein frequency per meter of quartz veins at Shadan; (b) contour plot of the total vein volume per cubic meter of quartz veins. The crosshatching is the zone with mineralized veins.

5.4. Litho geochemistry

A total of 360 rock samples were collected for litho geochemical analysis and were crushed, powdered, and analyzed by fire assay. Figure 10a depicts the histograms for Au that demonstrate that the concentration distributions of Au are positively skewed and exhibit a range of magnitudes. Statistical results show that Au mean and median values are 0.16 and 0.07 ppm, respectively. The concentration-number fractal model was adopted because it has a wide application in earth sciences [65–68]. Au concentrations were divided into three populations using a C–N fractal model, with grades ranging from below 0.15 ppm to between 0.15 and 0.35 ppm and greater than 0.35 ppm, respectively (Figure 10b). The geochemical map of Au was generated with the IDS (Inverse Distance Squared) method. The geochemical spatial distribution mapped by inverse distance weighted (IDW) in ArcGIS 10.8 exhibits the NW–SE trending Au mineralization and two separate anomalies (Figure 10c).

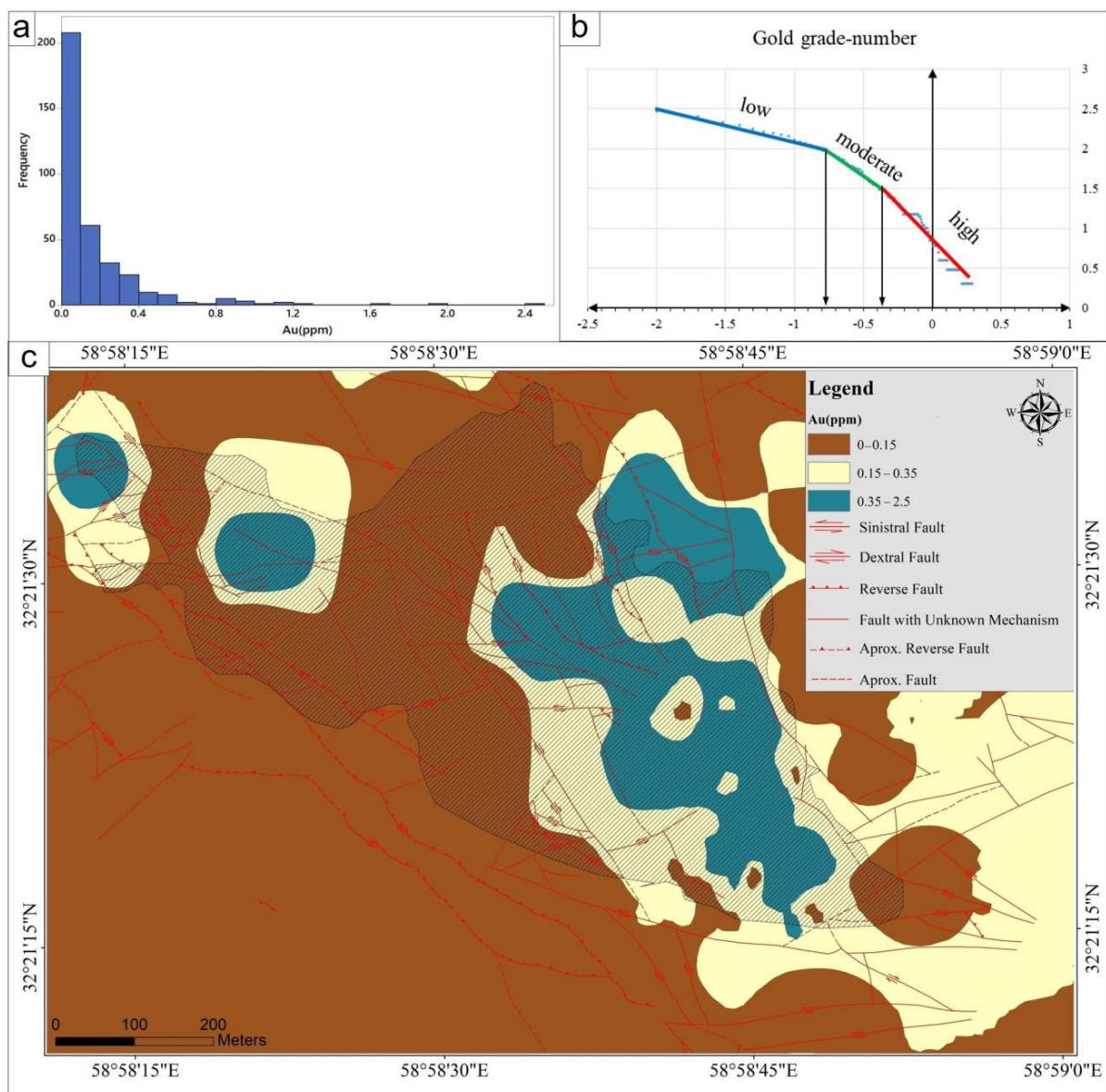


Figure 10. (a) Histograms of Au assay data, (b) C–N curve of Au assay data, (c) contoured Au geochemical assay population distribution (surface) map.

6. Discussion

6.1. Vein Emplacement Controller

The results in our study provide important information on the development of fractures in the Shadan deposit and a direct insight into the evolution of the mechanical states of hydrothermal systems. The sharp boundary between sheeted veins and their host rocks are evidence of the episodic release of magmatic fluids, after the emplacement of the porphyritic intrusions. Sheeted fractures as dilatant fractures cooperate in the transportation of ore-forming fluids from the deep magmatic source to the higher crustal levels. According to studies, sub-horizontal sheeted veins are formed prior to sub-vertical sheeted veins. Sub-horizontal sheeted veins point out a vertical extension component (dilatancy) during mineralization. A local change in deformation geometry or a change in fluid pressures could have generated vertical extension [69]. Textural evidence suggests a change in fluid pressure found in intrusions [70] and hydrothermal veins [71,72]. Consequently, some sub-horizontal fractures were formed, followed by sub-vertical fractures as result of hydraulic-driven extension superimposed onto them. In this case, early fractures formed as compressional shear fractures. Transpressional faults could intermittently prevent the expulsion of hydrothermal fluids, favoring the accumulation of volatiles in the magma chamber [64,73–76]. Subsequently, volatiles were released and channeled by transpressional faults, related to local or regional stress reversals.

6.2. Implications for Mineral Exploration Targeting

In the Shadan district, lithogeochemical anomalies were combined with vein density and vein volume maps to determine favorable areas for pioneer boreholes. In this manner, a concentration–area (C–A) fractal model was used to determine the threshold values of vein density and vein volume classes. The C–A fractal model on was calculated a log–log plot using power-law correlations, where inflection points showed various statistical populations. Straight-line parts were fitted in conformity with inflection points to prepare a set of cut-off values for subdividing the concentration scale into discrete classes [77]. On the basis of the inflection points of the area diagram versus the value, three classes of low, moderate, and high V.D and V.V were obtained (Figure 11). On the basis of the C–A fractal model on a log–log plot, three classes of low, moderate, and high V.D and V.V were obtained. High areas were reclassified as high potential zones and were compared with a high gold grade map. The overlapping of high-grade gold and high V.D/high V.V maps indicated favorable zones for drilling exploratory pioneer boreholes (Figure 12).

To evaluate high grade Au anomalies and high V.D/high V.V maps, the term “productivity” was applied to a more precise definition of good and poor boreholes. The following formula is used to define the productivity of each borehole [78]:

$$\text{Productivity} = \text{Mean (\%)} \times \text{Thickness (m)}$$

The threshold value (cut-off = 0.3 ppm) corresponds to the economic cut-off value for Au grade in ore reservoir modeling. As indicated in Table 1, low productivity boreholes are located on only Au anomalies (e.g., BH16, BH56, and BH62). In contrast, high productivity boreholes (e.g., BH05 and BH14) are located on the overlapping of Au anomalies and high V.D/high V.V areas. However, it should be noted that BH56 has same productivity with BH14, but gold mineralization of BH56 is a result of some scatter gold (nugget effect gold based on mineralogical studies), which in this case may not be mineable (Figure 13) due to the low thickness of the gold mineralization in contrast to the wall height in open pit mines [79,80].

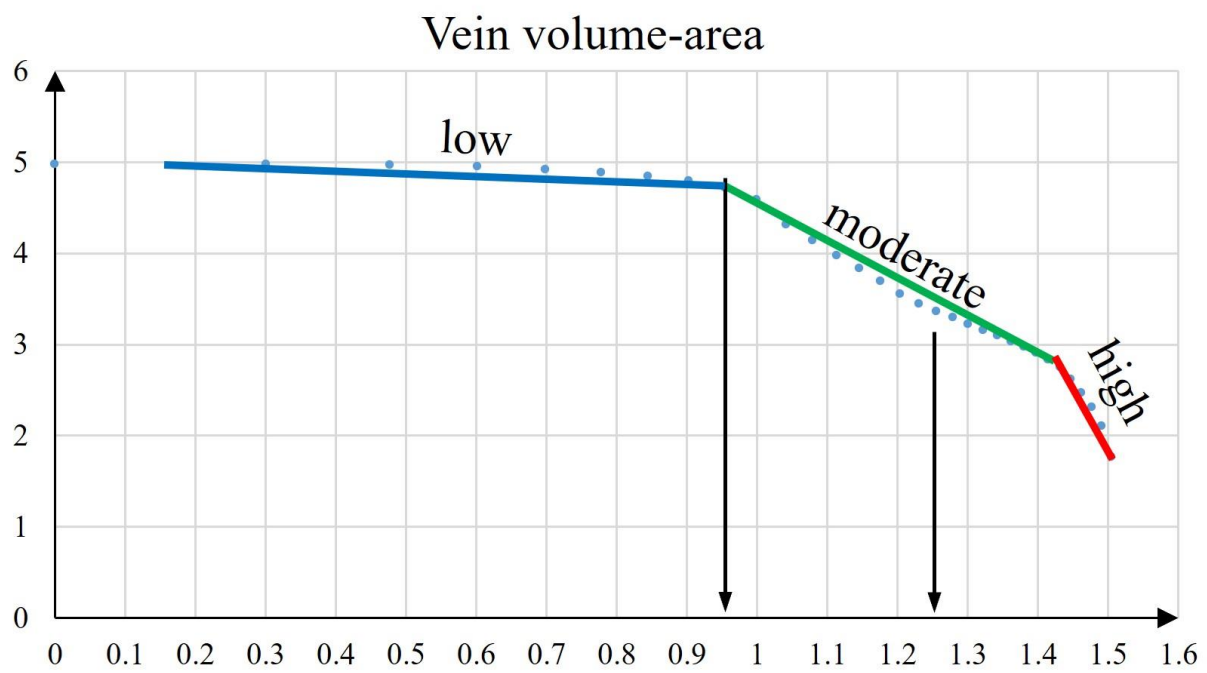
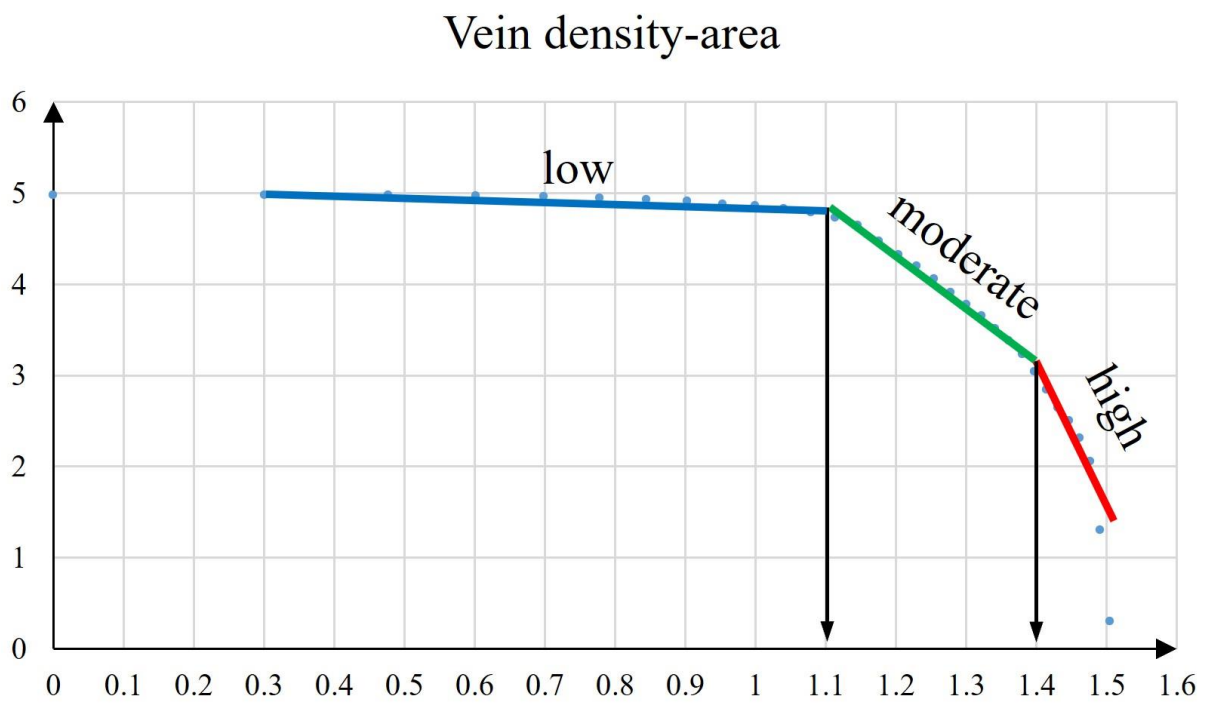


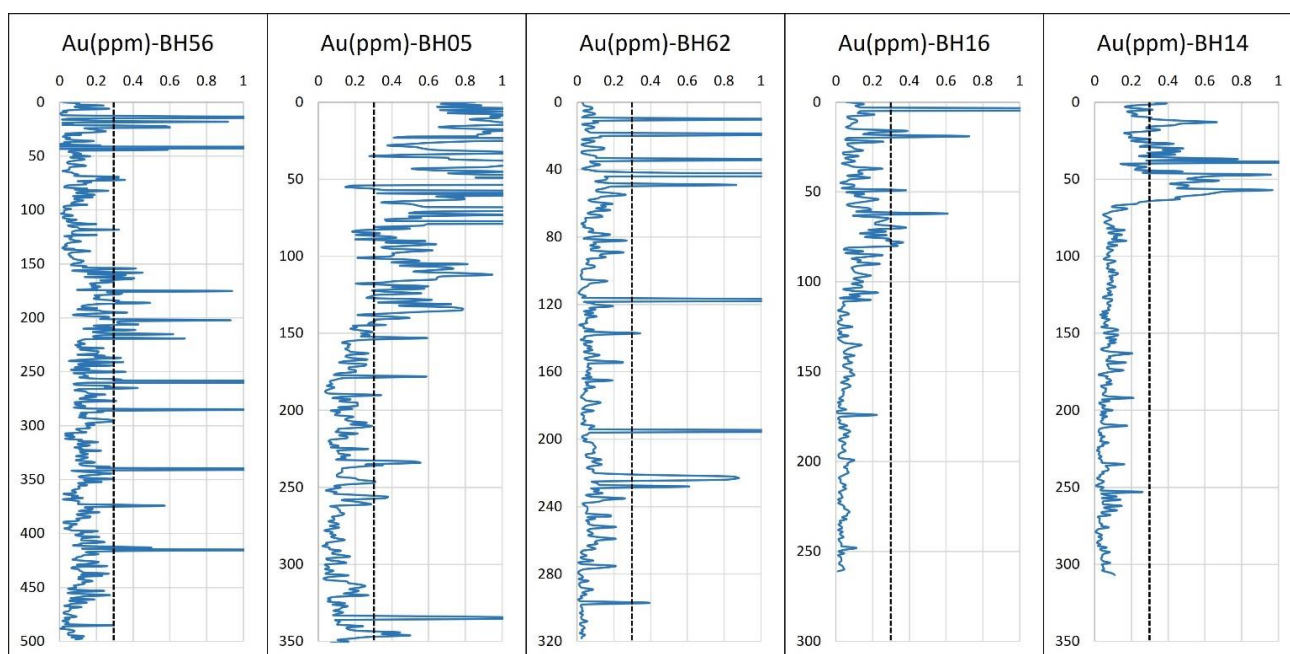
Figure 11. Log-log plots (C-A method) for vein density and vein volume.



Figure 12. Lithochemical gold anomalies map and location of boreholes located on anomalies.

Table 1. Borehole productivity.

BH Name	Mean (Cut Off = 0.3 g/t)	Thickness (Cut Off = 0.3 g/t)	Mean × Thickness (Cut Off = 0.3 g/t)
BH05	0.81	143	115.83
BH14	0.52	39	20.28
BH16	0.43	10	4.30
BH56	0.44	48	21.12
BH62	0.92	15	13.80

**Figure 13.** Gold grade (g/t) variation in boreholes drilled in potential zones. Dashed lines indicated economic cut-off value (Au = 0.3 g/t) for gold in the Shadan deposit.

7. Conclusions

Deep-seated misoriented faults provided the most favorable structural control for porphyry deposit within the Lut Block. The structural control is the same with that of the Cenozoic porphyry deposits of northern and central Chile [64]. These faults, under compression, inhibited ore-forming fluids from escaping, leading to volatile magma chamber accumulation to the point where rupturing results. Transpressional faults could be a key exploration criterion for PCDs targeting at the regional scale. The results highlight the important role of fault, vein, and fracture studies in porphyry exploration. Vein morphology, frequency, distribution, and orientations combined with other findings of geology, alteration, and deposit data (e.g., lithochemical data) are useful tools in exploration, especially in potential mineral mapping at the deposit scale.

Author Contributions: Conceptualization, D.R. and S.H.; methodology, D.R. and S.H.; software, D.R. and S.H.; validation, D.R.; S.H. and S.B; formal analysis, D.R. and S.H.; investigation, D.R. and S.H. and S.B.; resources, D.R. and S.H.; data curation, D.R. and S.H.; writing—original draft preparation, D.R. and S.H.; writing—review and editing, D.R.; S.H.; E.H.; S.B; M.S. and D.R.L.; visualization, D.R.; S.H.; supervision, D.R.; project administration, S.H. All authors have read and agreed to the published version of the manuscript.

Funding: This research received no external funding.

Acknowledgments: The authors gratefully acknowledge the management of Karand-Sadr Jahan Co. and the Shadan mine's management for their logistical supports. Mohammad Parsa kindly reviewed an earlier version of this manuscript, and we are very grateful for suggestions and helpful discussions on this paper.

Conflicts of Interest: The authors declare no conflict of interest.

References

1. Yousefi, M.; Kreuzer, O.P.; Nykänen, V.; Hronsky, J.M.A. Exploration information systems—A proposal for the future use of GIS in mineral exploration targeting. *Ore Geol. Rev.* **2019**, *111*, 103005. [[CrossRef](#)]
2. Saein, L.D.; Afzal, P. Correlation between Mo mineralization and faults using geostatistical and fractal modeling in porphyry deposits of Kerman Magmatic Belt, SE Iran. *J. Geochem. Explor.* **2017**, *181*, 333–343. [[CrossRef](#)]
3. Mohammadpour, M.; Bahroudi, A.; Abedi, M. Automatic Lineament Extraction Method in Mineral Exploration Using CANNY Algorithm and Hough Transform. *Geotectonics* **2020**, *54*, 366–382. [[CrossRef](#)]
4. Pahlavani, P.; Riahi, S.; Bigdeli, B. Ranking potentially favorable mineralization zones using fuzzy VIKOR vs. Dempster-Shafer-fuzzy AHP methods, a case study: Southeast of the Sarcheshmeh copper mine, Kerman, Iran. *Arab. J. Geosci.* **2020**, *13*, 1–21. [[CrossRef](#)]
5. Gustafson, L.B.; Hunt, J.P. The porphyry copper deposit at El Salvador, Chile. *Econ. Geol.* **1975**, *70*, 857–912. [[CrossRef](#)]
6. Sillitoe, R.H. Porphyry copper systems. *Econ. Geol.* **2010**, *105*, 3–41. [[CrossRef](#)]
7. Burnham, C.W. Magmas and hydrothermal fluids. In *Geochemistry of Hydrothermal Ore Deposits*, 2nd ed.; Barnes, H.L., Ed.; Wiley: New York, NY, USA, 1979; pp. 71–136.
8. Cline, J.S.; Bodnar, R.J. Direct evolution of brine from a crystallizing silicic melt at the Questa, New Mexico, molybdenum deposit. *Econ. Geol.* **1994**, *89*, 1780–1802. [[CrossRef](#)]
9. Shinohara, H.; Hedenquist, J.W. Constraints on magma degassing beneath the Far Southeast porphyry Cu–Au deposit, Philippines. *J. Petrol.* **1997**, *38*, 1741–1752. [[CrossRef](#)]
10. Harris, A.C.; Holcombe, R.J. Quartz vein emplacement mechanisms at the E26 porphyry Cu–Au deposit, New South Wales. *Econ. Geol.* **2014**, *109*, 1035–1050. [[CrossRef](#)]
11. Haynes, F.M.; Titley, S.R. The evolution of fracture-related permeability within the Ruby Star Granodiorite, Sierrita porphyry copper deposit, Pima County, Arizona. *Econ. Geol.* **1980**, *75*, 673–683. [[CrossRef](#)]
12. Heidrick, T.L.; Titley, S.R. Fracture and dike patterns in Laramide plutons and their structural and tectonic implications. In *Advances in Geology of the Porphyry Copper Deposits, Southwestern North America*; University of Arizona Press: Tucson, AZ, USA, 1982; pp. 73–91.
13. Titley, S.R.; Thompson, R.C.; Haynes, F.M.; Manske, S.L.; Robison, L.C.; White, J.L. Evolution of fractures and alteration in the Sierrita-Esperanza hydrothermal system, Pima County, Arizona. *Econ. Geol.* **1986**, *81*, 343–370. [[CrossRef](#)]
14. Tosdal, R.M. Magmatic and structural controls on the development of porphyry Cu±Mo±Au deposits. *Rev. Econ. Geol.* **2001**, *14*, 157–181.
15. Richards, J.P. Tectono-magmatic precursors for porphyry Cu-(Mo-Au) deposit formation. *Econ. Geol.* **2003**, *98*, 1515–1533. [[CrossRef](#)]
16. Richards, J.P.; Sholeh, A. The Tethyan Tectonic History and Cu-Au Metallogeny of Iran. In *2016 Tectonics and Metallogeny of the Tethyan Orogenic Belt*; Richards, J.P., Ed.; SEG Special Publication: Houston, TX, USA, 2016; Volume 19, pp. 193–212.
17. Cloos, M.; Sapiie, B. Porphyry copper deposits: Strike-slip faulting and throttling cupolas. *Int. Geol. Rev.* **2013**, *55*, 43–65. [[CrossRef](#)]
18. Swanson, M.T. Extensional duplexing in the York Cliffs strike-slip fault system, southern coastal Maine. *J. Struct. Geol.* **1990**, *12*, 499–512. [[CrossRef](#)]
19. Drew, L.J.; Berger, B.R.; Bawiec, W.J.; Sutphin, D.M.; Csirik, G.; Korpás, L.; Vetö-Akos, E.; Odor, L.; Kiss, J. Mineral resource assessment of the Mátra and Börzöny-Visegrád Mountains, North Hungary. *Geol. Hung.* **1999**, *24*, 79–96.
20. Henley, R.W.; Berger, B.R. Nature's refineries—Metals and metalloids in arc volcanoes. *Earth-Sci. Rev.* **2013**, *125*, 146–170. [[CrossRef](#)]
21. Shafiei, B.; Haschke, M.; Shahabpour, J. Recycling of orogenic arc crust triggers porphyry Cu mineralization in Kerman Cenozoic arc rocks, southeastern Iran. *Miner. Depos.* **2009**, *44*, 265–283. [[CrossRef](#)]
22. Safari, H.O.; Bagas, L.; Bafti, B.S. Structural controls on the localization of Cu deposits in the Kerman Cu metallogenic province of Iran using geoinformatic techniques. *Ore Geol. Rev.* **2015**, *67*, 43–56. [[CrossRef](#)]
23. Amiri Hanza, H.; Shafieibafti, S.; Derakhshani, R.; Khojastehfar, S. Controls on Cu mineralization in central part of the Kerman porphyry copper belt, SE Iran: Constraints from structural and spatial pattern analysis. *J. Struct. Geol.* **2018**, *116*, 159–177. [[CrossRef](#)]
24. Richards, J.P.; Spell, T.; Rameh, E.; Raziq, A.; Fletcher, T. High Sr/Y magmas reflect arc maturity, high magmatic water content, and porphyry Cu±Mo±Au potential: Examples from the Tethyan arcs of central and eastern Iran and western Pakistan. *Econ. Geol.* **2012**, *107*, 295–332. [[CrossRef](#)]

25. Mahdavi, P.; Jafari Rad, A.; Heuss-Aßbichler, S.; Lotfi, M.; Nezafati, N. Geology, mineralogy, and fluids inclusion studies in Shadan copper-gold deposit, Southern Khorasan. *Geopersia* **2020**, *10*, 263–275.
26. Siahcheshm, K.; Calagari, A.A.; Abedini, A. Hydrothermal evolution in the Maher-Abad porphyry Cu–Au deposit, SW Birjand, Eastern Iran: Evidence from fluid inclusions. *Ore Geol. Rev.* **2014**, *58*, 1–13. [[CrossRef](#)]
27. Alavi, M. *Tectonic Map of the Middle East*; Scale 1:5,000,000; Geological Survey of Iran: Tehran, Iran, 1981.
28. Berberian, M.; King, G.C.P. Towards a paleogeography and tectonic evolution of Iran. *Can. J. Earth Sci.* **1981**, *18*, 210–265. [[CrossRef](#)]
29. Nabavi, M.H. An introduction to the geology of Iran. In *The Economic Geology of Iran*; Springer: Dordrecht, The Netherlands, 1976.
30. Ramezani, J.; Tucker, R.D. The Saghand region, central Iran: U–Pb geochronology, petrogenesis and implications for Gondwana tectonics. *Am. J. Sci.* **2003**, *303*, 622–665. [[CrossRef](#)]
31. Stocklin, J.; Nabavi, M.H. Tectonic map of Iran. *Geol. Surv. Iran* **1973**, *1*, 5.
32. Camp, V.E.; Griffis, R.J. Character, genesis and tectonic setting of igneous rocks in the Sistan suture zone, eastern Iran. *Lithos* **1982**, *15*, 221–239. [[CrossRef](#)]
33. Tirrul, R.; Bell, I.R.; Griffis, R.J.; Camp, V.E. The Sistan suture zone of eastern Iran. *Geol. Soc. Am. Bull.* **1983**, *94*, 134–150. [[CrossRef](#)]
34. Tarkian, M.; Lotfi, M.; Baumann, A. Tectonic, Magmatism and the Formation of Mineral Deposits in the Central Lut, East Iran. *Minist. Mines Met. Geol. Surv. Iran Geodyn. Proj.* **1983**, *51*, 357–383.
35. Verdel, C.; Wernicke, B.P.; Hassanzadeh, J.; Guest, B. A Paleogene extensional arc flare-up in Iran. *Tectonics* **2011**, *30*. [[CrossRef](#)]
36. Saccani, E.; Delavari, M.; Beccaluva, L.; Amini, S. Petrological and geochemical constraints on the origin of the Nehbandan ophiolitic complex (eastern Iran): Implication for the evolution of the Sistan Ocean. *Lithos* **2010**, *117*, 209–228. [[CrossRef](#)]
37. Arjmandzadeh, R.; Karimpour, M.H.; Mazaheri, S.A.; Santos, J.F.; Medina, J.M.; Homam, S.M. Sr–Nd isotope geochemistry and petrogenesis of the Chah-Shaljami granitoids (Lut Block, eastern Iran). *J. Asian Earth Sci.* **2011**, *41*, 283–296. [[CrossRef](#)]
38. Arjmandzadeh, R.; Santos, J.F. Sr–Nd isotope geochemistry and tectonomagmatic setting of the Dehsalm Cu–Mo porphyry mineralizing intrusives from Lut Block, eastern Iran. *Int. J. Earth Sci.* **2014**, *103*, 123–140. [[CrossRef](#)]
39. Miri Beydokhti, R.; Karimpour, M.H.; Mazaheri, S.A.; Santos, J.F.; Klötzli, U. U–Pb zircon geochronology, Sr–Nd geochemistry, petrogenesis and tectonic setting of Mahoor granitoid rocks (Lut Block, Eastern Iran). *J. Asian Earth Sci.* **2015**, *111*, 192–205. [[CrossRef](#)]
40. Nakhaei, M.; Mazaheri, S.A.; Karimpour, M.H.; Stern, C.R.; Zarrinkoub, M.H.; Mohammadi, S.S. Geochronologic, geochemical, and isotopic constraints on petrogenesis of the dioritic rocks associated with Fe skarn in the Bisheh area, Eastern Iran. *Arab. J. Geosci.* **2015**, *8*, 8481–8495. [[CrossRef](#)]
41. Samiee, S.; Karimpour, M.H.; Ghaderi, M.; Shahri, M.R.H.; Klötzli, U.; Santos, J.F. Petrogenesis of subvolcanic rocks from the Khunik prospecting area, south of Birjand, Iran: Geochemical, Sr–Nd isotopic and U–Pb zircon constraints. *J. Asian Earth Sci.* **2016**, *115*, 170–182. [[CrossRef](#)]
42. Hosseinkhani, A.; Karimpour, M.H.; Shafaroudi, A.M.; Santos, J.F. U–Pb geochronology and petrogenesis of intrusive rocks: Constraints on the mode of genesis and timing of Cu mineralization in SWSK area, Lut Block. *J. Geochem. Explor.* **2017**, *177*, 11–27. [[CrossRef](#)]
43. Omidianfar, S.; Monsef, I.; Rahgoshay, M.; Zheng, J.; Cousens, B. The middle Eocene high-K magmatism in Eastern Iran Magmatic Belt: Constraints from U–Pb zircon geochronology and Sr–Nd isotopic ratios. *Int. Geol. Rev.* **2020**, *62*, 1751–1768. [[CrossRef](#)]
44. Karand Saderjahan Co. Report on completing exploratory operations in Shadan ore. *Geopersia* **2015**, *10*, 263–275. (In Persian)
45. Shafiei, B.; Shahabpour, J. Gold distribution in porphyry copper deposits of Kerman region, Southeastern Iran. *J. Sci. Islam. Repub. Iran* **2008**, *19*, 247–260.
46. Kirkham, R.V.; Dunne, K.P. World distribution of porphyry, porphyry-associated skarn, and bulk-tonnage epithermal deposits and occurrences. *Geol. Surv. Can. Open File* **2000**, 3792, 26.
47. Sillitoe, R.H. A plate tectonic model for the origin of porphyry copper deposits. *Econ. Geol.* **1972**, *67*, 184–197. [[CrossRef](#)]
48. Liang, H.Y.; Sun, W.; Su, W.C.; Zartman, R.E. Porphyry copper-gold mineralization at Yulong, China, promoted by decreasing redox potential during magnetite alteration. *Econ. Geol.* **2009**, *104*, 587–596. [[CrossRef](#)]
49. Sulaksono, A.; Watanabe, Y.; Arribas, A.; Echigo, T.; Al Furqan, R.; Leys, C.A. Reduction of oxidized sulfur in the formation of the Grasberg porphyry copper-gold deposit, Papua, Indonesia. *Miner. Depos.* **2021**, *56*, 1027–1042. [[CrossRef](#)]
50. Afzal, P.; Eskandarnejad Tehrani, M.; Ghaderi, M. Delineation of supergene enrichment, hypogene and oxidation zones utilizing staged factor analysis and fractal modeling in Takht-e-Gonbad porphyry deposit, SE Iran. *J. Geochem. Explor.* **2016**, *161*, 119–127. [[CrossRef](#)]
51. Carranza, E.J.M. Controls on mineral deposit occurrence inferred from analysis of their spatial pattern and spatial association with geological features. *Ore Geol. Rev.* **2009**, *35*, 383–400. [[CrossRef](#)]
52. Daneshvar Saein, L.; Rasa, I.; Rashidnejad Omran, N.; Moarefvand, P.; Afzal, P. Application of concentration-volume fractal method in induced polarization and resistivity data interpretation for Cu–Mo porphyry deposits exploration, case study: Nowchun Cu–Mo deposit, SE Iran. *Nonlinear Process. Geophys.* **2012**, *19*, 431–438. [[CrossRef](#)]
53. Gumiel, P.; Sanderson, D.J.; Arias, M.; Roberts, S.; Martín-Izard, A. Analysis of the fractal clustering of ore deposits in the Spanish Iberian Pyrite Belt. *Ore Geol. Rev.* **2010**, *38*, 307–318. [[CrossRef](#)]

54. Soltani, F.; Afzal, P.; Asghari, O. Delineation of alteration zones based on Sequential Gaussian Simulation and concentration–volume fractal modeling in the hypogene zone of Sungun copper deposit, NW Iran. *J. Geochem. Explor.* **2014**, *140*, 64–76. [[CrossRef](#)]
55. Mandelbrot, B.B. *The Fractal Geometry of Nature*; W.H. Freeman and Company: New York, NY, USA, 1983; p. 468.
56. Sadeghi, B.; Moarefvand, P.; Afzal, P.; Yasrebi, A.B.; Saein, L.D. Application of fractal models to outline mineralized zones in the Zaghia iron ore deposit, Central Iran. *J. Geochem. Explor.* **2012**, *122*, 9–19. [[CrossRef](#)]
57. Cheng, Q.; Agterberg, F.P.; Ballantyne, S.B. The separation of geochemical anomalies from background by fractal methods. *J. Geochem. Explor.* **1994**, *51*, 109–130. [[CrossRef](#)]
58. Cheng, Q. Spatial and scaling modelling for geochemical anomaly separation. *J. Geochem. Explor.* **1999**, *65*, 175–194. [[CrossRef](#)]
59. Li, C.; Ma, T.; Shi, J. Application of a fractal method relating concentrations and distances for separation of geochemical anomalies from background. *J. Geochem. Explor.* **2003**, *77*, 167–175. [[CrossRef](#)]
60. Afzal, P.; Fadakar, A.Y.; Khakzad, A.; Moarefvand, P.; Rashidnejad, O.N. Delineation of mineralization zones in porphyry Cu-deposits by fractal concentration volume modeling. *J. Geochem. Explor.* **2011**, *108*, 220–232. [[CrossRef](#)]
61. Hassanpour, S.; Afzal, P. Application of concentration–number (C–N) multifractal modeling for geochemical anomaly separation in Haftcheshmeh porphyry system, NW Iran. *Arab. J. Geosci.* **2013**, *6*, 957–970. [[CrossRef](#)]
62. Sadeghi, B.; Madani, N.; Carranza, E.J.M. Combination of geostatistical simulation and fractal modeling for mineral resource classification. *J. Geochem. Explor.* **2015**, *149*, 59–73. [[CrossRef](#)]
63. Rezaei, S.; Lotfi, M.; Afzal, P.; Jafari, M.R.; Meigoony, M.S. Delineation of Cu prospects utilizing multifractal modeling and stepwise factor analysis in Noubaran 1: 100,000 sheet, Center of Iran. *Arab. J. Geosci.* **2015**, *8*, 7343–7357. [[CrossRef](#)]
64. Piquer, J.; Sanchez-Alfaro, P.; Pérez-Flores, P. A new model for the optimal structural context for giant porphyry copper deposit formation. *Geology* **2021**, *49*, 597–601. [[CrossRef](#)]
65. Mao, Z.; Peng, S.; Lai, J.; Shao, Y.; Yang, B. Fractal study of geochemical prospecting data in south area of Fenghuanshan copper deposit, Tongling Anhui. *J. Earth Sci. Environ.* **2004**, *26*, 1–14.
66. Hassanpour, S.; Senemari, S.; Roomi, N. Delineation of mineralization zones by multivariate fractal and zonality modeling in south of the Sungun and Kighal porphyry systems, NW, Iran. *Arab. J. Geosci.* **2022**, *15*, 703. [[CrossRef](#)]
67. Kurdi, M.; Soltani-Mohammadi, S.; Eslamkish, T.; Larina, N. Evaluating the performance of concentration-number (C–N) fractal model for separation of soil horizon regarding vertical distribution and 3D models. *J. Tethys* **2017**, *5*, 337–349.
68. Darvishi, M.T.; Najafi, N.; Wazwaz, A.M. Conformable space-time fractional nonlinear (1+1)-dimensional Schrödinger-type models and their traveling wave solutions. *Chaos Solitons Fractals* **2021**, *150*, 111187. [[CrossRef](#)]
69. Gudmundsson, A. How local stresses control magma-chamber ruptures, dyke injections, and eruptions in composite volcanoes. *Earth-Sci. Rev.* **2006**, *79*, 1–31. [[CrossRef](#)]
70. Lickfold, V.; Cooke, D.R.; Smith, S.G.; Ullrich, T.D. Endeavour copper-gold porphyry deposits, Northparkes, New South Wales: Intrusive history and fluid evolution. *Econ. Geol.* **2003**, *98*, 1607–1636. [[CrossRef](#)]
71. Redmond, P.B.; Einaudi, M.T.; Inan, E.E.; Landtwing, M.R.; Heinrich, C.A. Copper deposition by fluid cooling in intrusion-centered systems: New insights from the Bingham porphyry ore deposit, Utah. *Geology* **2004**, *32*, 217–220. [[CrossRef](#)]
72. Müller, A.; Herrington, R.; Armstrong, R.; Seltmann, R.; Kirwin, D.J.; Stenina, N.G.; Kronz, A. Trace elements and cathodoluminescence of quartz in stockwork veins of Mongolian porphyry-style deposits. *Miner. Depos.* **2010**, *45*, 707–727. [[CrossRef](#)]
73. Spinks, K.D.; Acocella, V.; Cole, J.W.; Bassett, K.N. Structural control of volcanism and caldera development in the transtensional Taupo Volcanic Zone, New Zealand. *J. Volcanol. Geotherm. Res.* **2005**, *144*, 7–22. [[CrossRef](#)]
74. Cembrano, J.; Lara, L. The link between volcanism and tectonics in the southern volcanic zone of the Chilean Andes: A review. *Tectonophysics* **2009**, *471*, 96–113. [[CrossRef](#)]
75. Tardani, D.; Reich, M.; Roulleau, E.; Takahata, N.; Sano, Y.; Pérez-Flores, P.; Sánchez-Alfaro, P.; Cembrano, J.; Arancibia, G. Exploring the structural controls on helium, nitrogen and carbon isotope signatures in hydrothermal fluids along an intra-arc fault system. *Geochim. Cosmochim. Acta* **2016**, *184*, 193–211. [[CrossRef](#)]
76. Cabaniss, H.E.; Gregg, P.M.; Grosfils, E.B. The role of tectonic stress in triggering large silicic caldera eruptions. *Geophys. Res. Lett.* **2018**, *45*, 3889–3895. [[CrossRef](#)]
77. Thiombane, M.; Martin-Fernandez, J.A.; Albanese, S.; Lima, A.; Doherti, A.; De Vivo, B. Exploratory analysis of multi-element geochemical patterns in soil from the Sarno River Basin (Campania region, southern Italy) through compositional data analysis (CODA). *J. Geochem. Explor.* **2018**, *195*, 110–120. [[CrossRef](#)]
78. Hosseini, S.A.; Abedi, M. Data envelopment analysis: A knowledge-driven method for mineral prospectivity mapping. *Comput. Geosci.* **2015**, *82*, 111–119. [[CrossRef](#)]
79. Sahandi, M.R.; Soheili, M. Geological and structural zonation map of Iran. *Geol. Surv. Iran* **2014**, *56*, 263–287.
80. Raeisi, D.; Zhao, M.; Babazadeh, S.; Long, L.E.; Hajsadeghi, S.; Modabberi, S. Synthesis on productive, sub productive and barren intrusions in the Urumieh-Dokhtar magmatic arc, Iran, constrains on geochronology and geochemistry. *Ore Geol. Rev.* **2021**, *132*, 103997. [[CrossRef](#)]

Disclaimer/Publisher’s Note: The statements, opinions and data contained in all publications are solely those of the individual author(s) and contributor(s) and not of MDPI and/or the editor(s). MDPI and/or the editor(s) disclaim responsibility for any injury to people or property resulting from any ideas, methods, instructions or products referred to in the content.